# Nanoscale

Accepted Manuscript


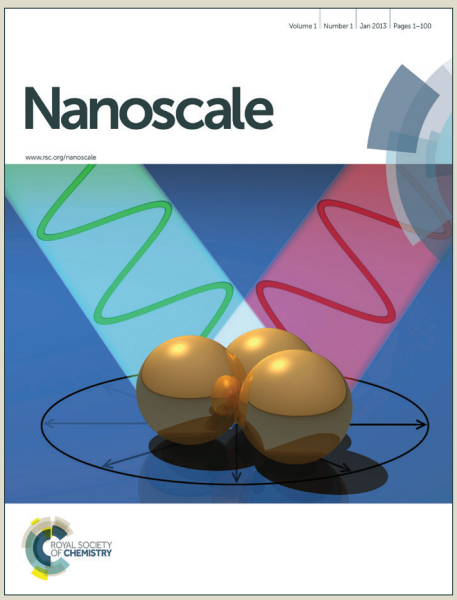





ROYAL SOCIETY OF CHEMISTRY

www.rsc.org/nanoscale

# Ultrafast and scalable photochemical synthesis of tin oxide nanotubes with mesoporous nanocrystals and their application in lithium ion batteries

*Zhikun Liu*[+,1], *Zeyuan Cao*[+,3], *Biwei Deng*[1], *Yuefeng Wang*[2], *Jiayi Shao*[2], *Prashant Kumar*[1], *C. Richard Liu*[1], *Bingqing Wei*[*3], *Gary J. Cheng*[*,1,2]

([+] Both authors contributed equally to the paper.)

[1]Industrial Engineering, Purdue University, West Lafayette, Indiana, 47907, USA.
[2]Birck Nanotechnology Centre, Purdue University, West Lafayette, Indiana, 47907, USA.
[3]Department of Mechanical Engineering, University of Delaware, Newark, DE, 19716, USA

* Corresponding authors, E-mails: gjcheng@purdue.edu and weib@udel.edu

**Keywords:** Tin oxide nanotubes, Laser manufacture, Photochemical synthesis, Electrochemical properties, Lithium ion batteries.

## Abstract

Laser-induced photo-chemical synthesis of $SnO_2$ nanotubes has been demonstrated by employing nanoporous polycarbonate membrane as a template. The $SnO_2$ nanotube diameter can be controlled by the nanoporous template while the nanotube length can be tuned by laser parameters and reaction duration. The microstructure characterization of the nanotubes indicates that they consists of mesoporous structures with sub-5nm size nanocrystals connected by the twinning structure. The applications of $SnO_2$ nanotubes as an anode material in lithium ion batteries have also been explored, which exhibited a high capacity and an excellent cyclic stability. The laser based emerging technique for scalable production of crystalline metal oxide nanotubes in matter of seconds is remarkable. The compliance of the laser based technique with the existing technologies would lead to mass production of novel nanomaterials that would suit for several emerging applications.

Production of nanomaterials at large scale and at fast pace is the demand of the time as nanotechnology based industries are flourishing and adding new production lines. For better

device functionality, one needs to have nanostructures with better spatial uniformity in size, high crystallinity and integration. Most of the presently available techniques employed for the synthesis of nanowires involve multiple steps and are time consuming. Therefore, novel approaches to satisfy the needs of emerging nano-devices are being developed and so as the scalable production of the device components.

Lithium ion batteries[1-6] are attracting more attention from industry because of the high energy density and compactness. Tin oxide ($SnO_2$) nanotubes, as a promising anode material for lithium ion batteries [7-10] can be synthesized via either chemical or physical approaches [11-18]. However, the dimension control, purity and scalability are still issues yet to be addressed. Precision nanomanufacturing of tin oxide nanotubes would therefore be a crucial step towards their energy applications. Lasers are capable of delivery of high energy density in an instantaneous manner and have earlier been exploited for the pursuit of material synthesis[19-28], which makes them an appropriate and suitable choice for on-demand, ultrafast production of nanoarchitectures such as nanowires, nanotubes, nanodots, etc. Laser processing has brought many discoveries and novel approaches in material synthesis with added advantages such as scalability and a fast processing speed.

We hereby demonstrate a laser based approach for the ultrafast photo-chemical synthesis of tin oxide nanotubes by employing polycarbonate membrane as a template (Fig. 1a). It is worthy noting that the present technique is not limited to tin oxide only but many materials, and therefore, this emerging technique being flexible, would pave the ways to nanomanufacture nanostructures of many functional material systems. As an example, the electrochemical performance of the $SnO_2$ nanotubes synthesized by the laser based photochemical technique has also been investigated, which exhibit an excellent cyclic stability with high rate capability and a high capacity close to the theoretical value.

Lucrative aspect of the present technique is that it provides the freedom to write lines and patterns of vertically aligned nanowires, simply by irradiates the laser along a desired path onto the polycarbonate membrane template. Such a degree of freedom and scalability would be beneficial for patterned nanowire growth which is usually desired for battery devices. Fig. 1(b) shows one of such laser written tracks. Figs. 1(c) and 1(d) are FESEM images of the microstructures inside and outside the laser written track, respectively. In brief, Fig. 1(c) shows a dense, uniform, and vertically aligned $SnO_2$ nanotube array on the sputtered gold thin film. This image was captured after the polycabrbonate nanoporous template was dissolved in the dichloromethane solvent. The height and diameter of the nanotubes are approximately 4 μm and 450 nm, respectively. Nanotube diameter can conveniently be controlled by nanopore's diameter in polycarbonate nanoporous template. Inset in Fig. 1(c) is a plot of average nanotube length vs. laser power. Laser power proves to be a good control parameter for the nanotube length.

Nanotubes fabricated with the present technique have typically thin walls. TEM image in Fig. 2(a) showing nanotubes with wall thickness of about 14 nm confirms it. In order to investigate the nanotube formation and to develop a deeper understanding, we have examined the bottom part of the nanotube formed, which would reveal the early stage of growth features of the nanotubes. The selected area electron diffraction (SAED) pattern from the $SnO_2$ nanotubes exhibit diffraction rings corresponding to [110], [101] and [301] crystallographic planes as shown in Fig. 2 (a). Figs. 2(b)-(f) show the details of the $SnO_2$ nanotube formation. As is apparent from HRTEM image of the bottom of the nanotubes, growth of $SnO_2$ nanotube begins with ultrafine 2 nm diameter $SnO_2$ nanoparticles (see Fig. 2(b)). Fig. 2(c) depicts the formation of mesopores (2-5 nm in diameter). The image in Fig. 2(d) reveals that the

nanoparticles are connected by the twinning structure, which is a typical microstructure at the early stage of nanoparticle coalescence.

When a laser pulse is absorbed by the Au back plate, the irradiated area becomes the heating source for the solution. Since heating at bottom of the solution generates fluid convection within the channel, the heat transfer of the solution is governed by conduction and convection. Comsol Multiphysics simulation has been carried out that is capable of coupling both heat transfer and laminar flow in solution (Conjugate Heat Transfer mode). Fig 2 (e) is a simulation result showing temperature modulation by a laser pulse at the location 1 μm above the back plate within the channel. The temperature gradually rises up to 390 K within the pulse duration of 400 ns. After the laser pulse is off, the conduction and convection of the fluid cools down the temperature within 200 ns. The cooling rate after the laser pulse is switched off is estimated to be at the scale of 5 x $10^8$ K/s, which is a very rapid cooling rate.

The synthesis of the $SnO_2$ nanotubes in the present technique can easily be understood in terms of laser-induced photo-chemical decomposition of precursors and consequent crystallization. The heating of the solution leads to stronger ionization of water. The exponential increase of concentration of $OH^-$ results in the supersaturation of $Sn(OH)_4$. $SnO_2$ is then formed by laser-induced dehydration of $Sn(OH)_4$. The formation of nanocrystalline $SnO_2$ has been confirmed from the diffraction pattern in Fig. 2(a) and the high resolution TEM of Fig. 2(d).

$$Sn^{4+} + 4(OH)^- \rightarrow Sn(OH)_4 \quad (1)$$

$$Sn(OH)_4 \xrightarrow{laser\ heating} SnO_2 + 2H_2O \quad (2)$$

Nucleation and growth occur within nanosecond time span as La Mer model[29] for the laser-induced crystallization in such photo-chemical reaction, as demonstrated in Fig. 2(f). It is

noted in Fig. 2(f) that nucleation can be controlled by nitric acid concentration and which have been experimentally observed. For example, for solution containing 180 mM nitric acid, fine nanoparticles of 2 nm diameter formed, while the nanoparticles of 3 nm diameter formed when nitric acid concentration is reduced to 50 mM.

Such laser-induced crystallization of monodispersed ultrafine nanoparticles is very interesting from the crystallization point of view, as the time needed for the crystallization process is only a few hundred nanoseconds. According to La Mer's model, it is necessary to distinguish the nucleation stage and growth process in timescale in order to achieve a nanocrystal size distribution close to a monodisperse level. As the concentration of hydroxide ions gradually increases above the equilibrium solubility, the nucleation of $Sn(OH)_4$ bursts out when the supersaturation achieves a definite value. Let $C_{nucleation}$ be the critical concentration of the $OH^-$ to trigger nucleation. As soon as laser is switched off, within a short duration, the nucleation process commences and the temperature quickly drops. At the concentration below $C_{nucleation,}$ nuclei formation would not be favored. Now, if the duration of nucleation is minimal, monodispersed nanoparticles can be achieved[30]

After the Region II, the crystal growth would proceed till the concentration of growth species has reduced to the equilibrium concentration $C_{growth}$. Further reduction of the $OH^-$ ions into Region IV brings the particle growth into a halt. The duration of time between the commencement of nucleation and the finish point for crystal growth is denoted as $\tau$. The duration $\tau$ of the photochemical process in the present technique is estimated to be at the scale of $10^{-7}$ s. A smaller $\tau$ value generally favors ultrafine monodispersed nanocrystal growth. In addition, usually the fast cooling rate favors monodispersity in nanoparticle size, even under a wide range of activation energy of crystallization. The cooling rate in the present case of laser-induced photo-chemical transformation is estimated to be at the scale of $5 \times 10^8$ K/s.

Also, it should be noted that majority of the laser energy is utilized in photochemical reactions and therefore, residual laser power is not able to give rise to thermal rise. In addition, aqueous background does not allow laser pulses to create abnormal thermal spike and helps maintain a low background temperature. This is in contrast to usual laser crystallization techniques where the material undergoes through a thermal spike and a moderate cooling rate, which give rise to larger crystals[31]

Thus, the present photo-chemical technique which yields monodisperse ultrafine nanocrystals relies on the deterministic factors: (a) adequate concentration of growth species, (b) marginalized $OH^-$ ion concentration, (c) low background temperature due to liquid ambient, and (d) supercooling. All of these deterministic the factors lead to spontaneous crystal growth with negligible duration and yield monodisperse ultrafine nanocrystals when a particular set of the above factors are created. If the reaction is forced to halt at the moment close to the commencement, one would achieve such monodisperse ultrafine nanocrystals. It has to be noted that the size of the $SnO_2$ nanocrystals achieved in the present work is one of the thinnest nanosized-$SnO_2$ ever synthesized. From materials point of view, such ultrafine quantum confined semiconducting nanodots (quantum dots) would exhibit fascinating and unusual physical behavior.

The present technique to photo-chemically synthesize inorganic nanotubes, employing nanoporous cylindrical template presents a novel approach towards fabrication of nanotubes in a scalable manner. The formation of tubular structure (see Fig. 3(a)) instead of the solid wire structure can be understood by the fluid convection initiated by the bubbling. To study the mechanism of the $SnO_2$ nanotube formation, a control experiment has been carried out by heating the entire solution uniformly at 95$^oC$ on a hotplate for 10 min. The SEM image shows very short gel-like columns instead of tubes as shown in Fig.3(c). The inset of the Fig. 3(c) is

the diffraction pattern of the short columns. The absence of the ring patterns suggests that the column is composed of amorphous $Sn(OH)_4$. Laser induced local heating thus plays two crucial roles in the nanotube formation. The first is the laser-induced convection for the formation of the desired tubular structure and the second is the laser dehydration of $Sn(OH)_4$. As discussed earlier, laser local heating generates temperature gradient in the solution. Hotter solution at the bottom of channel will float up and is replaced by the cold solution. The fluid convection by the buoyancy difference is simulated using the Comsol Multiphysics and shown in Figs. 3(b) and 3(d). During the laser pulse, the hot fluid flows upward at the center of channel while the solution is static at the interface to the polycarbonate membrane because of the none slippery boundary condition. The convection at the center of channel will prevent the formation of column structure and keep the tubular structure during the growth. The tubular structure formed by laser-induced photo-chemical synthesis is shown in Fig. 3(a). The relative rigid network of the $SnO_2$ nanocrystals prevents the collapse of the thin-wall tubular structures after the polycarbonate template is dissolved. As shown in Fig. 1(b), we have demonstrated that laser can be employed to write patterns consisting of segments, which are constituted by vertically aligned freestanding $SnO_2$ nanotubes. Such patterned features can find incredible importance in device design and manufacturing.

The large surface area inherited from the colloid of $SnO_2$ particles can facilitate lithium reaction and therefore, $SnO_2$ nanotubes would act as a nice platform for lithiation. Furthermore, the tubular structures could serve as channels for lithium ion transport to shorten the $Li^+$ diffusion length efficiently and to enhance the charge transfer process along the axial direction. To explore seemingly advantageous electrochemical aspect of the $SnO_2$ nanotubes, the electrochemical measurements were performed. Fig. 4(a) presents the galvanostatic discharge/charge profiles of the $SnO_2$ nanotubes at the rate of 0.1 C for the selected cycles: the 1st, 2nd, 10th, 20th, and 100th cycle. The initial capacity of 2750 $mAhg^{-1}$ is quite

impressive in comparison to recent literature on lithium ion batteries made up of $SnO_2$/Sn systems[32] and $SnO_2$ nanotubes[33]. It is also noted from Fig. 4(a) that the capacity sharply drops to 1400 $mAhg^{-1}$, which is only half of the initial capacity after the first discharge. The irreversible loss of capacity is attributed to the formation of the solid electrolyte interface (SEI) and the decomposition of $SnO_2$ to Sn during the initial cycle. In the beginning the curves remain a similar shape with two distinct short plateaus at around 0.5 and 0.05 V corresponding to phase transition processes during Li+ insertion, which would be clarified in the following cyclic voltammetry (CV) analysis. Whereas, a variation occurs with the cycles: the plateau gradually disappears and the curves become a line with a steepened slope. It is indicative of a typical solid solution reaction by $Li^+$ insertion.

The cycling performance of the 100 cycles at 0.1 C (Fig. 4(b)) shows that the capacity is decreased linearly with a slope of 30 $mAhg^{-1}$/cycle in the first 20 cycles except initial discharge and evolving in a steady state since the $20^{th}$ cycle. The capacity retains about 600 $mAhg^{-1}$ at the end of the $100^{th}$ cycle while it was 818 $mAhg^{-1}$ at the $20^{th}$ cycle. The capacity degradation rate is about 2.75 $mAhg^{-1}$/cycle during the last eighty cycles. It is evident that the capacity and cyclic stability are improved exceptionally well as compared with the commercial $SnO_2$ nanopowders that usually fade quickly within 50 cycles. The electrochemical impedance spectra (EIS) in Fig. S1 (Supporting Information) for the four respective cycles ($1^{st}$, $5^{th}$, $25^{th}$ and $100^{th}$ cycle) also shows the similar Nyquist plots comprised by a depressed semicircle at a high frequency attributed to the charge-transfer process at the electrolyte/electrode interface and a linear tail named Warburg component at low frequencies corresponding to the $Li^+$ diffusion in the solid electrodes. Their knee frequency (intersection between the semicircle and Warburg tail) is at around 15 Hz close to each other and the similar charge-transfer resistances deduced from the radius of the semicircle reveal similar kinetics.

The CV curves in consecutive ten cycles are presented in Fig. 4(c). There are two well-defined cathodic peaks at around 0.05 V and 0.5 V for all the curves except for a broad peak in range of 0.5 – 2 V during the first cycle, which comes from the reduction of $SnO_2$ by $Li^+$ to Sn and formation of $Li_2O$ in Equation (3). This reaction accounts for the irreversible loss of capacity shown in Fig. 4(b). The peaks at 0.5 V and 0.05 V correspond to the formation of a series of Li-Sn alloys, $Li_xSn$ as described in Equation (4).

$$SnO_2 + 4\,Li^+ + 4\,e^- \rightarrow Sn + 2\,Li_2O \quad (3)$$

$$Sn + x\,Li^+ + x\,e^- \leftrightarrow Li_xSn\ (0 \le x \le 4.4) \quad (4)$$

In the anodic sweep, the two peaks at 0.55 V and 1.25 V are ascribed to the reversed dealloying processes of the Equation (4) mainly in two steps. All the four features related to the lithium insertion/extraction in Equation (4) are well overlapped with cycles, indicating the excellent reversible capacity of lithiation. This is in a good agreement with the previous results of capacity retention.

We also evaluated the electrochemical performance of the $SnO_2$ nanotubes in terms of the rate capability by means of galvanostatic discharge/charge cycling tests at a variety of high rates up to 10 C. The discharge/charge curves (Fig. 4(d)) shows that the tendency of variation with cycles becoming a smooth slope is facilitated under the large current densities. Neither plateaus nor inflection on the curve could be observed after the $40^{th}$ cycle at 4 C. The overall cycling performance at different rates (Figure (e)) have similar trend as was found for the experiment at constant rate of 0.1 C. When raising the minimum rate of 0.1 C to the maximum 10 C and back to 0.5 C, the corresponding Coulombic efficiency is varying from 93 % to 99 % and returning back to 98%.

The histogram (Fig 4(f)) visually exhibits the comparison of the average capacity at various rates. The mean value of the capacities in the first five cycles at 0.1 C is 1500 $mAhg^{-1}$ which is highest of all. The values for 0.5 C, 1 C, 2 C, 4C, 8C and 10 C were observed to be 998 $mAhg^{-1}$, 715 $mAhg^{-1}$, 560 $mAhg^{-1}$, 448 $mAhg^{-1}$, 361 $mAhg^{-1}$, and 324 $mAhg^{-1}$, respectively. The capacity of 324 $mAhg^{-1}$ at 10 C, which was performed within 6 min. is an encouraging result. In the last 10 cycles back to the low rate of 0.5 C, the capacity recovers to about 600 $mAhg^{-1}$ on average, further confirming the excellent cyclic stability of the $SnO_2$ nanotubes.

Since the structural integrity throughout the cycling tests ensures the good cyclability, the morphology variation of the $SnO_2$ nanotube electrodes over continuous discharge/charge cycles at 0.1 C has been studied by means of SEM. Although the nanotubes experience deformation obviously with enlarged sizes and curled edges, only a small bunch of tubes are fully collapsed as marked in Fig. S2 (a); and tubes are rarely found cracked (Fig. S2 (b)). Many initially isolated and vertically standing $SnO_2$ nanotubes are aggregated to bundles by the SEI layers wrapped along the tube walls as highlighted in Fig. S2 (d). From the top view of the nanotubes (Figs. S2 (c) and S2 (e)), it is easy to find that the ultrafine nanoparticles are still intact together to constitute the tube walls after cycling. The hollow tubes are filled with Li-Sn alloy during lithium insertion, which could be seen from the interior of the nanotubes cracked along the generating line of the cylinder in Fig. S2 (f).

In summary, laser-induced photo-chemical technique to synthesize $SnO_2$ nanotubes has been demonstrated. Diameter of the nanotubes can be tuned by nanoporous template dimension and the length of the nanotube can be controlled by laser pulse irradiation duration and laser power. The growth of $SnO_2$ nanotubes is catalyzed by laser heated hot zones on a gold back plate. Laser triggered photo-chemical reactions of precursors in aqueous environment, which yields fast cooling and results in the formation of ultrafine $SnO_2$ nanocrystals. These ultrafine $SnO_2$ nanocrystals assemble themselves in rings and thus in turn nanotubes are built up by

vertical alignment of such ultrafine nanocrystals. Heat convection plays an important role by creating favorable experimental conditions. This emerging photo-chemical synthesis of nanotubes can conveniently be generalized to other material systems and nanostructures. Patterning capability of such laser-based photochemical fabrication technique has also been demonstrated. Instantaneous synthesis of inorganic nanotubes in a scalable manner with the achievement of high quality material crystallinity makes this novel technique very unique. Lithium ion batteries were fabricated using the $SnO_2$ nanotubes synthesized by this emerging technique and electrochemical performance was observed to be better than other $SnO_2$ based nanosystems.

**Experimental Section**

Focused laser beam (Q-switch long-pulse Nd-YAG fiber laser of wavelength 532 nm and pulse width 200 ns) of beam size of 1 mm has been irradiated on a transparent solution (25 mM $SnCl_4$ and 180 mM $HNO_3$) lying above a nanoporous membrane [polycarbonate nanoporous template with 400 nm pore size (Whatman® Polycarbonate membrane filter, 7 μm thick)], which was back-coated by 50 nm gold thin film. The experimental set-up for the present approach is shown in Fig. 1(a). The gold thin film absorbs the laser energy, heats up a certain amount of chemical solution and thereby initiates the chemical reaction needed for the growth of the $SnO_2$ nanotubes. The laser can cover millions of nanopores in a single scan. When the growth of nanotubes finished, a 1 μm thick layer of copper was electrodeposited onto the top of the Au thin film to provide required mechanical support. The polycarbonate nanoporous template is then dissolved by dichloroethane and the vertically aligned $SnO_2$ nanotubes are achieved. Field emission scanning electron microscopy (FESEM) and transmission electron microscopy (TEM) have been employed for characterizing the nanoshapes formed. Comsol Multiphysics simulation has been carried out to investigate and

understand the nanotube growth process. To be specific, two different simulations have been performed namely, (a) thermal profiling of the photo-chemical process in time scale, which has yielded $SnO_2$ nanotubes and (b) convection of heat inside the interior space in the nanoporous template, with and without flow. The electrochemical measurements were performed in a coin cell configuration consisting of the as-prepared $SnO_2$ nanotubes without any post-treatment as the working electrode, a metallic Li as the counter and reference electrode. The Celgard 2500 were chosen as separators and 1 M $LiPF_6$ dissolved in 1:1 v/v ethylene carbonate (EC): diethyl carbonate (DEC) were used as electrolyte obtained from Ferro Co. The cyclic voltammetry (CV) measurements and electrochemical impedance spectra (EIS) were collected by PARSTAT 2273 (Princeton Applied Research) potentiostat/galvanostat. CV was carried out at a scan rate of 0.1 $mVs^{-1}$ in the potential window of 0 - 3 V to identify the electrochemical reactions with lithium during cycling. EIS was performed with a 10 mV AC signal from 100 kHz to 10 mHz. The galvanostatic discharge-charge tests were carried out using BT-4 4-channel battery test equipment (Arbin Instrument, ltd.).

**Acknowledgements**

Authors would like to acknowledge financial support from Purdue Office of Vice President for Research. BQW gratefully acknowledges the financial support from the US National Science Foundation (NSF) under the contract of 1067947.

**References:**

[1] J.-M. Tarascon, M. Armand, *Nature*, 2001, **414**, 359-367.

[2] A. S. Aricò, P. Bruce, B. Scrosati, J.-M. Tarascon, W. V. Schalkwijk, *Nature Mater.*, 2005, **4**, 366 – 377.

[3] B. Scrosati. *Electrochim. Acta*, 2000, **45**, 2461–2466.

[4] N. Li, C. R. Martin, B. Scrosati. *J. Power Sources*, 2001, **97**, 240–243.

[5] P. Poizot, S. Laruelle, S. Grugeon, L. Dupont & J-M. Tarascon. *Nature,* 2000, **407**, 496-499.

[6] B. Scrosati, J. Hassoun, Y.-K. Sun. *Energy Environ. Sci.*, 2011, **4**, 3287-3295.

[7] Y. Idota, T. Kubota, A. Matsufuji, Y. Maekawa, T. Miyasaka. *Science*, 1997, **276**, 1395-1397.

[8] F. Belliard, P. A. Connor, J. T. S. Irvine. *Solid State Ionics*, 2000, **135**, 163–167.

[9] J. Y. Huang, L. Zhong, C. M. Wang, J. P. Sullivan, W. Xu, L. Q. Zhang, S. X. Mao, N. S. Hudak, X. H. Liu, A. Subramanian, H. Fan, L. Qi, A. Kushima, J. Li. *Science*, 2010, **330**, 1515-1520.

[10] M. -S. Park, G. -X. Wang, Y. –M. Kang, D. Wexler, S. –X. Dou, H. –K. Liu. *Angew. Chem. Int. Edit.* 2007, **119**, 764 –767.

[11] Y. Wang, X. Jiang, Y. Xia. *J. Am. Chem. Soc.,* 2003, **125**, 16176-16177.

[12] P. Meduri, C. Pendyala, V. Kumar, G. U. Sumanasekera, M. K. Sunkara. *Nano Lett.*, 2009, **9**, 612-616.

[13] J. Q. Hu, X. L. Ma, N. G. Shang, Z. Y. Xie, N. B. Wong, C. S. Lee, S. T. Lee. *J. Phys. Chem. B*, 2002, **106***,* 3823-3826.

[14] Z. R. Dai, J. L. Gole, J. D. Stout, Z. L. Wang. *J. Phys. Chem. B*, 2002, **106***,* 1274-1279.

[15] X. Jiang, Y. Wang, T. Herricks, Y. Xia. *J. Mater. Chem.,* 2004, **14**, 695-703.

[16] S. Luo, J. Fan, W. Liu, M. Zhang, Z. Song, C. Lin, X. Wu, P. K. Chu. *Nanotechnology*, 2006, **17,** 1695–1699.

[17] P. Parthangal, R. E. Cavicchi, D. C. Meier, A. Herzing, M. R. Zachariah. *J. Mater. Res.*, 2011, **26**, 430-436.

[18] G. Sberveglieri, I. Concina, E. Comini, M. Falasconi, M. Ferroni, V. Sberveglieri. *Vacuum*, 2012, **6**, 532 -535.

[19] A. M. Morales, C. M. Lieber. *Science*, 1998, **279**, 208-211.

[20] D. H. Lowndes, D. B. Geohegan, A. A. Puretzky, D. P. Norton, C. M. Rouleau. *Science*, 1996, **273**, 898-903.

[21] A. E. Espinal, L. Zhang, C.-H. Chen, A. Morey, Y. Nie, L. Espinal, B. O. Wells, R. Joesten, M. Aindow and S. L. Suib. *Nature Mater.*, 2010, **9**, 54-59.

[22] Z. Liu, D. Zhang, S. Han, C. Li, T. Tang, W. Jin, X. Liu, B. Lei, C. Zhou. *Adv. Mater.*, 2003, **15**, 1754-1757.

[23] V. V. Osipov, Y. A. Kotov, M. G. Ivanov, O. M. Samatov, V. V. Lisenkov, V. V. Platonov, A. M. Murzakaev, A. I. Medvedev, E. I. Azarkevich. *Laser Phys.*, 2006, **16**, 116–125.

[24] F. Kim, J. H. Song, P. Yang. *J. Am. Chem. Soc.,* 2002, **124**, 14316-14317.

[25] M. Sakamoto, M. Fujistuka, T. Majima. *J. Photoch. Photobio. C*, 2009, **10**, 33–56.

[26] V. S. Letokhov. *Appl. Phys. B*, 1988, **46**, 237-251.

[27] P. Kumar. *RSC Adv*., 2013, **3**, 11987-12002.

[28] S. Besner, M. Meunier, "Laser synthesis of nanomaterials" in "Laser precision microfabrication" (K. Sugioka et. al. (Eds.), Spinger Series in Materials Science, 135, DOI: 10.1007/978-3-642-10523-4_7 (2010).

[29] V. K. LaMer. *J. Am. Chem. Soc.*, 1950, **72**, 4847-4854.

[30] G. Cao, in "Nanostructures and nanomaterials, Synthesis, properties and applications, (2004), pp. 53 Imperial College Press, London, ISBN 1-86094-480-9.

[31] P. Kumar, M. G. Krishna. *Phys. Status Solidi A*, 2009, **207**, 947-954.

[32] K. Kravchyk, L. Protesescu, M. I. Bodnarchuk, F. Krumeich, M. Yarema, M. Walter, C. Guntlin, M. V. Kovalenko. *J. Am. Chem. Soc.*, 2013, **135**, 4199−4202.

[33] J. Ye, H. Zhang, R. Yang, X. Li, L. Qi. *Small*, 2010, **6**, 296–306.

**Figure Captions:**

**Fig. 1.** Schematic of the laser-induced photo-chemical synthesis of $SnO_2$ nanotubes, (b) laser track written on a substrate after the template removal, (c) vertically aligned $SnO_2$ nanotubes inside the laser track (inset shows laser power dependence of nanotube length) and (d) random features outside the track.

**Fig. 2.** HRTEM image showing (a) walls of nanotube formed (inset shows selected area electron diffraction pattern), (b) ultrafinefine $SnO_2$ nanocrystals formed at the gold backplate, (c) mesopores and (d) nanograins, coalescence twin boundaries and mesopores. (e) Simulated thermal profile with the time elapsed and (f) the La Mer model for the crystallization process.

**Fig. 3.** (a) The top view FESEM image of tubular structure achieved by laser-induced photo-chemical synthesis (inset shows diffraction pattern), (b) the Comsol Multiphysics result of the convection flow during the laser local heating, (c) the top view of short columnar structure by uniform hot plate heating at $95^oC$ and (d) the Comsol Multiphysics result indicating no fluid flow during the hot plate heating.

**Fig. 4.** (a) The discharge/charge profiles for $SnO_2$ nanotubes at different rates; (b) The capacity retention and Coulombic efficiency of $SnO_2$ nanotubes at various discharge/charge rates, (c) The histogram of the mean capacity at specific rates for the corresponding cycles in (b); and (d) the CV curves at selected cycles.

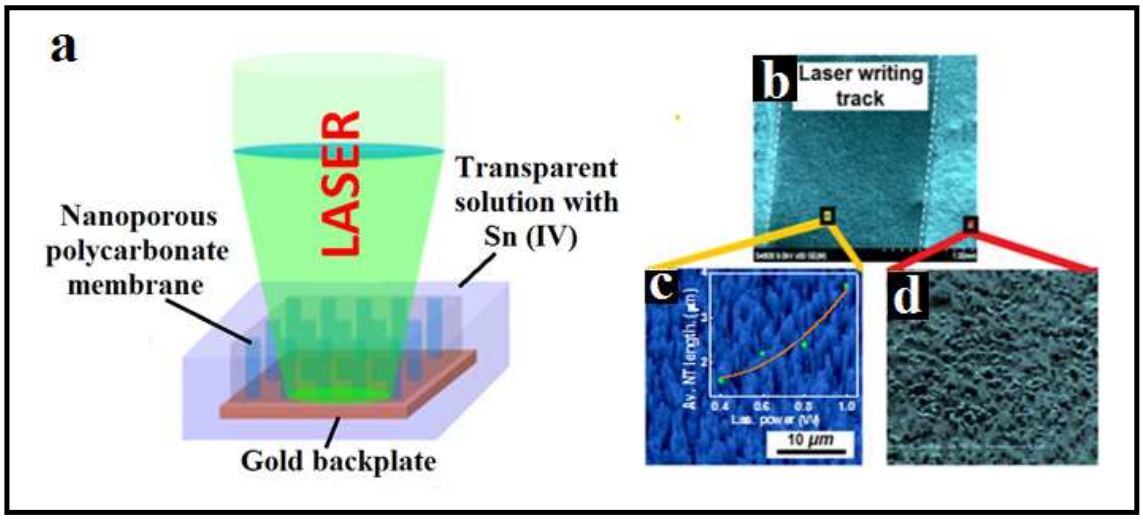


**Fig 1**

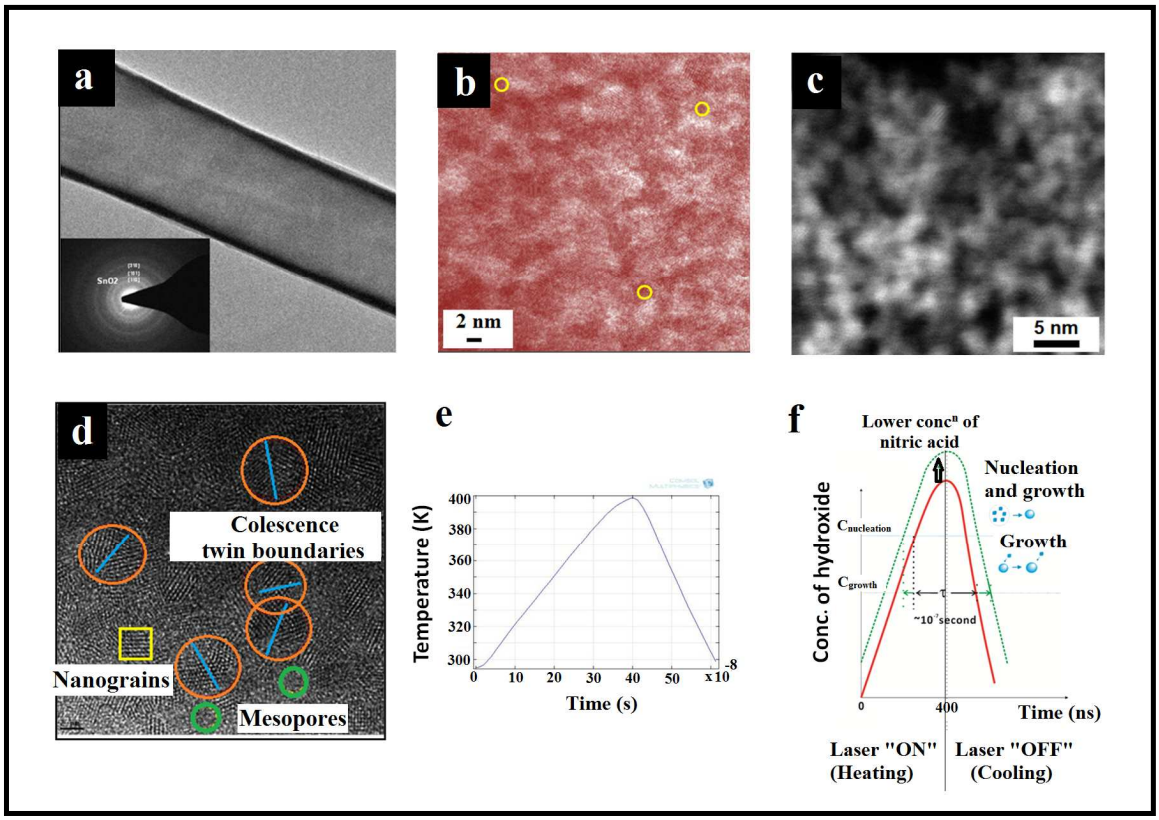


**Fig 2**

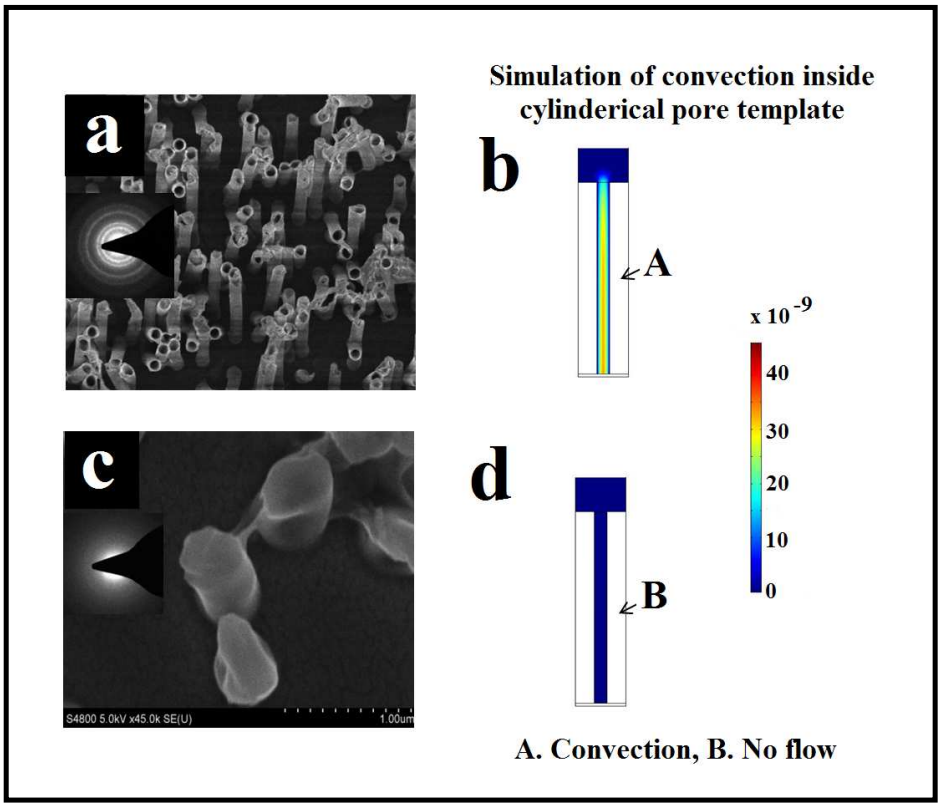


**Fig 3**

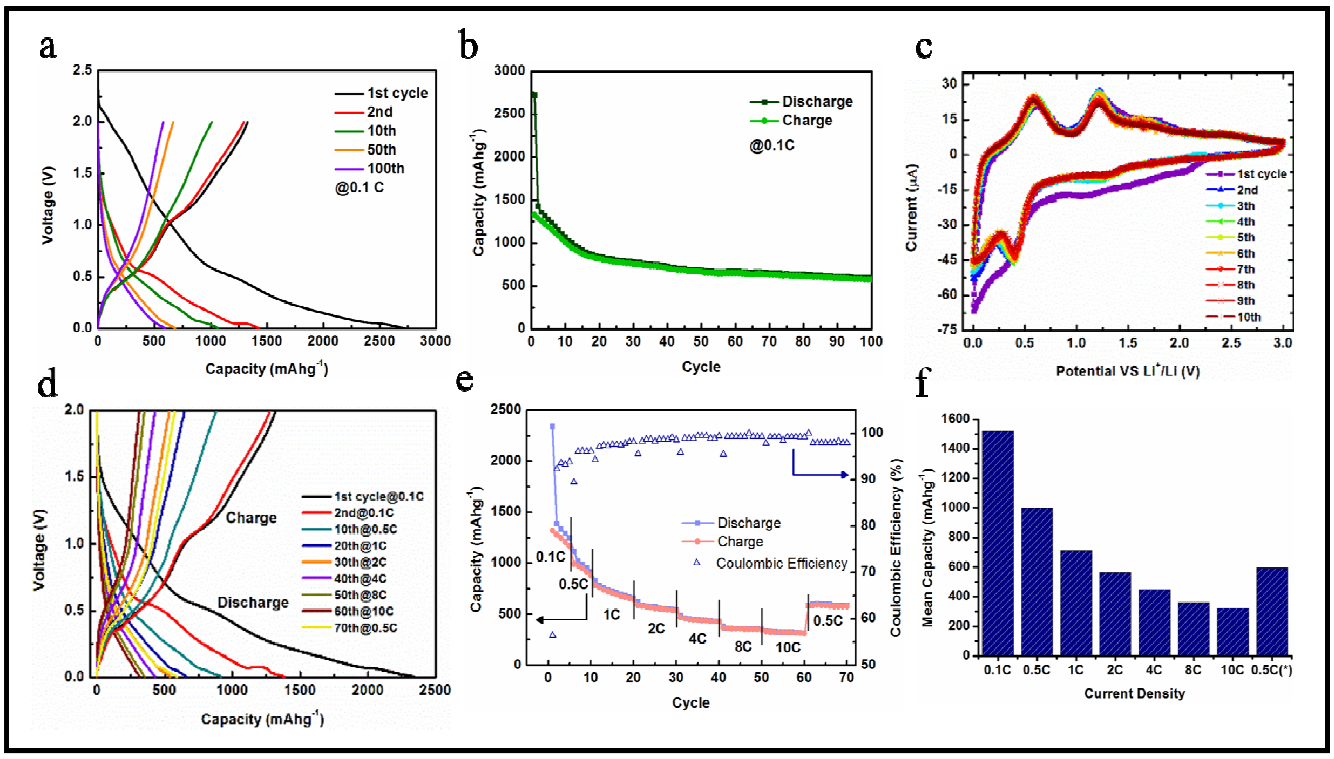


**Fig 4**

**The table of contents entry**
Laser-induced scalable and quick photo-chemical synthesis of tin oxide nanotubes has been illustrated and its application in lithium ion batteries has been investigated.

**Keyword** : Tin oxide nanotubes, Laser synthesis, Electrochemical properties.

Zhikun Liu+, Zeyuan Cao+, Prashant Kumar, Biwei Deng, Yuefeng Wang, C. Richard Liu*, Bingqing Wei*, Gary J. Cheng*

**Ultrafast and scalable photochemical synthesis of tin oxide nanotubes and its application in lithium ion batteries**

**TOC**

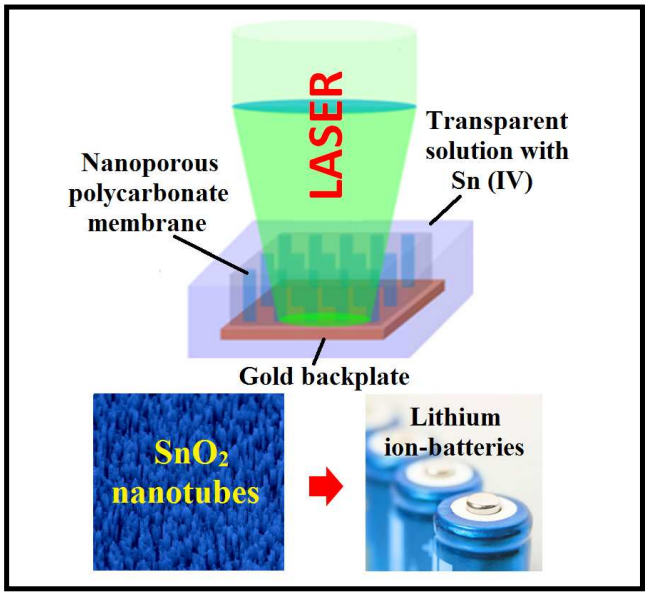

# Supporting Information

**Ultrafast and scalable photochemical synthesis of tin oxide nanotubes and its application in lithium ion batteries**

*Zhikun Liu[+], Zeyuan Cao[+], Prashant Kumar, Biwei Deng, Yuefeng Wang, C. Richard Liu, Bingqing Wei[*], Gary J. Cheng[*]*

**Figure captions**

**Fig. S1.** Comparison of Nyquist plots for the 1$^{nd}$, 5$^{th}$, 25$^{th}$ and 100$^{th}$ cycle at the rate of 0.1 C. Inset: the curves in full scale.

**Fig. S2.** SEM images of the $SnO_2$ nanotubes after continuous discharge/charge cycling at 0.1 C. (a) The marked area of collapsed nanotubes. (b) Cracked nanotubes. (c) The curled edges of nanotubes in magnified image. (d) Nanotube bundles by SEI layers. (e) Top view of a single $SnO_2$ nanotube. (f) Interior of a single cracked nanotube.

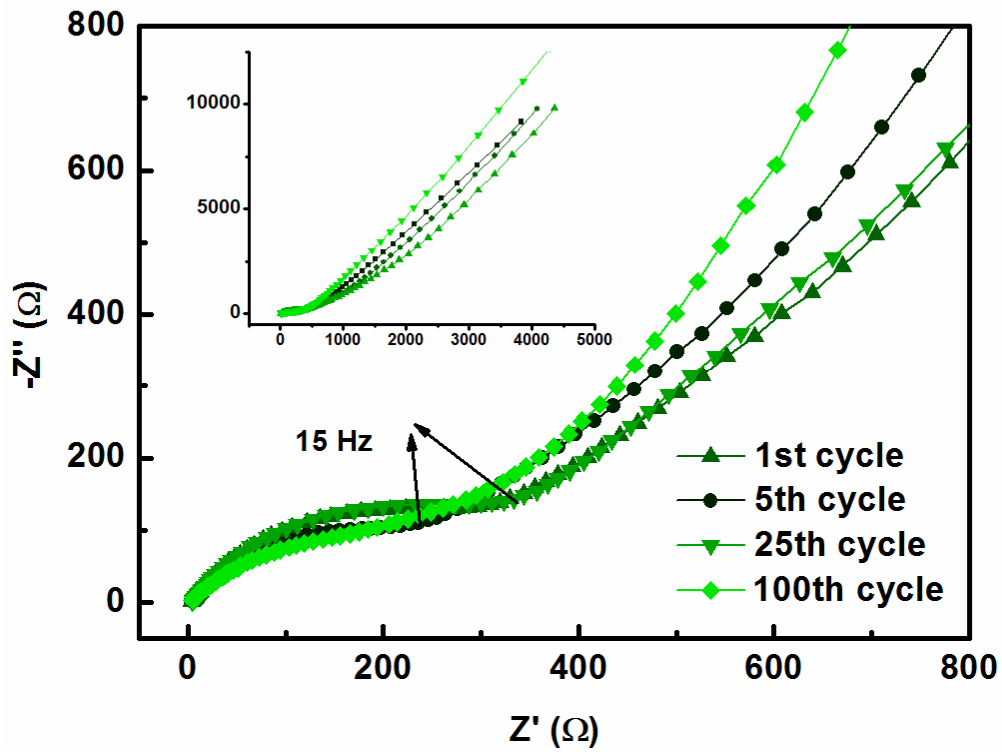


**Fig S1**

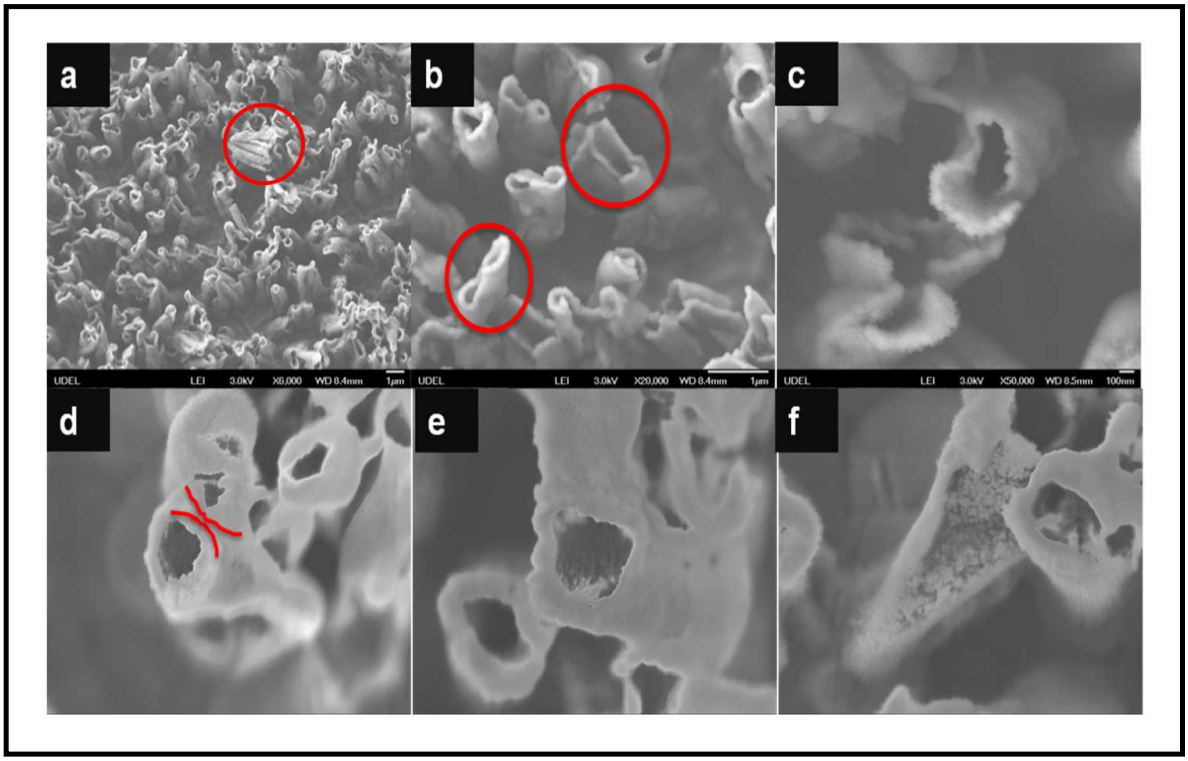


**Fig S2**